catalysts

MDPI

Article

Iron Carbide Nanoparticles Embedded in Edge-Rich, N and F Codoped Graphene/Carbon Nanotubes Hybrid for Oxygen Electrocatalysis

Xiaochang Qiao [1,2,*], Yijie Deng [3], Xiaochang Cao [4], Jiafeng Wu [1], Hui Guo [1], Wenhuang Xiao [1] and Shijun Liao [2,*]

[1] School of Materials Science and Engineering, Dongguan University of Technology, Dongguan 523808, China
[2] The Key Laboratory of Fuel Cell Technology of Guangdong Province, School of Chemistry and Chemical Engineering, South China University of Technology, Guangzhou 510641, China
[3] School of Resource Environmental and Safety Engineering, University of South China, Hengyang 421001, China
[4] School of Mechanical Engineering, Dongguan University of Technology, Dongguan 523808, China
* Correspondence: qiaoxc@dgut.edu.cn (X.Q.); chsjliao@scut.edu.cn (S.L.); Tel.: +86-20-871-1358 (S.L.)

Abstract: Rational design of cost-effective and efficient bifunctional oxygen electrocatalysts for sluggish oxygen reduction reaction (ORR) and oxygen evolution reaction (OER) is urgently desired for rechargeable metal–air batteries and regenerative fuel cells. Here, the Fe_3C nanoparticles encapsulated in N and F codoped and simultaneously etched graphene/CNTs architecture catalyst (Fe_3C@N-F-GCNTs) was synthesized by a simple yet cost-effective strategy. The as-prepared Fe_3C@N-F-GCNTs exhibited excellent ORR and OER performances, with the ORR half-wave potential positive than that of Pt/C by 14 mV, and the OER overpotential lowered to 432 mV at the current density of 10 mA·cm^{-2}. In addition, the ΔE value (oxygen electrode activity parameter) increased to 0.827 V, which is comparable to the performance of the best nonprecious metal catalysts reported to date. When it was applied in a Zn–air battery as a cathode, it achieved a peak power density of 130 mW·cm^{-2}, exhibiting the potential for large-scale applications.

Keywords: oxygen electrocatalyst; graphene/carbon nanotube; Fe_3C@C; N and F codoped; edge defects

Citation: Qiao, X.; Deng, Y.; Cao, X.; Wu, J.; Guo, H.; Xiao, W.; Liao, S. Iron Carbide Nanoparticles Embedded in Edge-Rich, N and F Codoped Graphene/Carbon Nanotubes Hybrid for Oxygen Electrocatalysis. *Catalysts* **2022**, *12*, 1023. https://doi.org/10.3390/catal12091023

Academic Editors: Jose Luis Diaz de Tuesta and Helder T. Gomes

Received: 10 August 2022
Accepted: 6 September 2022
Published: 9 September 2022

1. Introduction

Environmental friendly and sustainable energy conversion and storage systems, such as rechargeable metal–air batteries and fuel cells, are urgently required to effectively mitigate the current energy and environmental crisis [1,2]. However, their development and commercialization are hindered by the sluggish kinetics of oxygen reduction reaction (ORR) and oxygen evolution reaction (OER) [3]. To date, Pt-based materials are the most active catalysts for the ORR, while their OER activities are far from satisfactory. Ir- and Ru-based materials are widely used to accelerate the OER, whereas such catalysts exhibit insufficient ORR performance. Moreover, the pretty price, terrestrial scarcity, and low electrochemical durability of precious metals seriously limit their widespread applications [4]. Therefore, searching for an efficient way to fabricate low-cost, highly efficient, bifunctional oxygen electrocatalysts based on earth-abundant elements still remains a crucial challenge for researchers.

Recently, heteroatom-doped carbon-based materials have emerged as promising ORR/OER bifunctional electrocatalysts because of the reasonable balance among catalytic activity, stability, and cost [5–9]. Since the heteroatom (e.g., N, S, B, P, and F) and carbon atom have different electronegativity and atomic radius, the replacement of carbon atoms in graphitic carbon skeleton by heteroatoms can induce inhomogeneous electron distribution and efficiently modulate electron properties and introduce more active sites, thus boosting the bifunctional electrocatalytic oxygen activities [10,11]. Among various heteroatoms,

nitrogen has attracted more attention due to its similar atomic radius and five valence electrons for bonding with carbon atoms. Therefore, N atoms can be efficiently doped into a carbon matrix to enhance the oxygen electrode electrocatalytic activity. Moreover, compared with single N heteroatom doping, multi-heteroatoms codoped into a carbon skeleton can further improve the ORR/OER catalytic kinetic rates due to the synergistic effects arising from the codoped heteroatoms [12,13]. Since fluorine atom has the highest electronegativity, doping fluorine atoms can cause great surface polarization of the carbon matrix [8]. Therefore, because of the synergistic effect between N and F atoms leading to the maximum charge delocalization of C atoms, N and F codoped carbon materials have enhanced electrocatalytic activity [9,14–17]. In addition, 3D transition metal can promote the graphitization of carbon materials in the carbonization process, thus improving the electrical conductivity and strengthening the antioxidant capacity of the carbon-based catalysts [18]. At the same time, 3D transition metals are often the active components for oxygen electrocatalysis [19,20]. Moreover, 3D transition metals can catalyze carbon precursors to form carbon nanotubes or graphene [21,22]. The graphene/CNTs hybrid is considered as one of the most advanced carbon substrates for ORR/OER due to its corrosion resistance; high electrical conductivity; and special structure, which is conducive to the transmission of oxygen and removal of water [23,24]. In addition to heteroatom doping modification, defect engineering (such as etching or edging) of nanocarbon electrocatalysts could also effectively enhance their electrocatalytic activity in both experimental and theoretical studies [25,26]. However, etching of carbon materials is often prepared by a post-treatment method (such as laser etching or chemical activation) [27,28], and the preparation method is complicated.

In this study, we ingeniously choose polyvinylidene fluoride (PVDF), melamine, and iron acetate as precursors to in situ synthesis of Fe_3C encapsulated in edge-rich, N and F codoped graphene/carbon nanotubes hybrid electrocatalysts by an activation-free method. It is worth noting that the PVDF not only plays a role as a carbon and fluorine resource, but also could provide edge-sites and microporous structures by an activation-free method, as reported in the literature [29]. By taking advantage of the hierarchical porosity, enhanced electric conductivity, and the high density and multiple types of active sites, the resulting Fe_3C@N-F-GCNTs hybrid exhibits outstanding ORR and OER performance.

2. Results and Discussion

TEM and high-resolution TEM (HRTEM) images of Fe_3C@N-F-GCNTs, Fe-F-C, and N-F-C are shown in Figure 1 and Figure S1. Fe-F-C (Figure S1a,b) and N-F-C (Figure S1c,d) both exhibit graphenelike morphologies, while Fe_3C@N-F-GCNTs (Figure 1a,b) show an open 3D architecture coexisting of graphene and bamboolike carbon nanotubes. A large number of literatures have proved that the coexistence of melamine and iron salts is conducive to form a bamboolike, Fe_3C-encapsulated, carbon nanotubes structure [30–32]. The 3D architecture coexisting of graphene and bamboolike carbon nanotubes effectively inhibits the stacking of individual graphene sheets or carbon nanotubes, benefiting to expose more active sites, promote rapid electron transfer, and supply fast transport channels for O_2 diffusion and electrolyte infiltration, thereby improving the electrochemical performance. It can be seen that some nanosized holes on the surface of the graphene/CNTs substrate (partially highlighted with red open circles in Figure 1b,c) are generated in Fe_3C@N-F-GCNTs, resulting from the release of HF from the carbon chain in PVDF at high temperature under inert atmosphere or some metal particles on the surface getting leached out after subsequent acid treatment process [33]. It could also be confirmed by the TEM images of Fe-F-C and N-F-C (Figure S1), where the nanosized holes could also be seen on the graphene sheet's surface. Both edge effects and topological defects have been proved to be favorable for both ORR and OER [26,34]. HRTEM images (Figure 1d) show that Fe_3C nanoparticles are encapsulated in a 2.5 nm thick graphite carbon layer with a lattice spacing of 0.34 nm, corresponding to the (002) planes of graphitic carbon. The structure of the graphite carbon layer encapsulating the Fe_3C nanoparticles not only inhibits the dissolution

and agglomeration of the Fe_3C nanoparticles under the harsh alkaline/acidic solution, but also adjusts the electron density of the carbon surface to promote the surface catalytic reaction [10]. We further investigated the elemental distribution in Fe_3C@N-F-GCNTs using high-angle, annular, dark-field scanning TEM (HAADF-STEM). As shown in Figure 1e, all elements are evenly distributed throughout the sample except for the nanoparticle region. Two types of Fe species exist in the carbon matrix: one is atomically dispersed and the intensities of Fe and N match up to a certain degree, indicating that it may exist in the form of Fe-N_x, which is generally considered to be the active site of ORR; the other in the nanoparticle region has a few crystalline phases associated with Fe_3C, which has been proved by XRD.

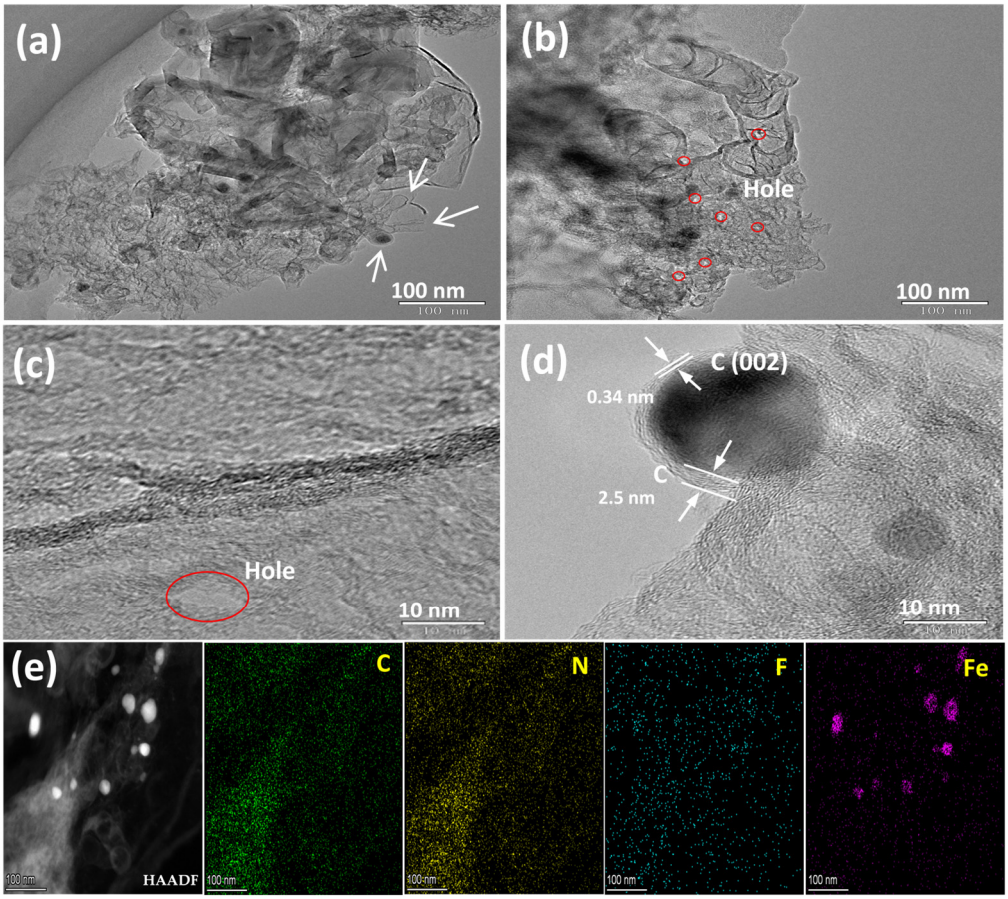

Figure 1. (**a**,**b**) TEM images and (**c**,**d**) HRTEM images of Fe_3C@N-F-GCNTs (the white arrows in (**a**) show the bamboolike carbon nanotubes formed; the nanoholes formed were labelled with red circles (**b**,**c**)); (**e**) HAADF-STEM image and corresponding elemental mapping images for Fe_3C@N-F-GCNTs.

Figure 2 shows the XRD patterns of Fe_3C@N-F-GCNTs, Fe-F-C, and N-F-C. All the XRD patterns show two broad diffraction peaks centered at 26.4° and 44.4°, corresponding to the (002) and (101) reflections of the graphitic peak, respectively (PDF#41-1487). It is noteworthy that the graphite peak of Fe_3C@N-F-GCNTs is much sharper and stronger than those of Fe-F-C and N-F-C, implying the higher graphitization of Fe_3C@N-F-GCNTs. The other diffraction peaks of Fe_3C@N-F-GCNTs were characteristic of Fe_3C (PDF#35-0772).

The N_2 adsorption–desorption isotherms (Figure 3a) were recorded to investigate the pore structure and surface area of Fe_3C@N-F-GCNTs. A typical type IV characteristic for the N_2 adsorption–desorption isotherms with hysteresis loops is observed, indicating the existence of plentiful mesopores. The BET surface area of Fe_3C@NF-GCNTs is 421 $m^2 \cdot g^{-1}$. The corresponding pore size distribution shows the coexistence of micropores, mesopores, and macropores (Figure 3b) and the pore volume is as high as 0.4 $cm^3 \cdot g^{-1}$. This result indicates

that the hierarchically porous structure has been successfully fabricated, which facilitates mass transport and active site exposure. As a contrast, the N_2 adsorption–desorption isotherm curves and the corresponding pore size distribution curves of N-F-C and Fe-F-C were also recorded. As shown in Figure S2a, the N_2 adsorption–desorption isotherms of the N-F-C have type I characteristics, with a steep initial region at P/P_0 = 0–0.03, indicating the catalyst's microporous structure. The corresponding pore size distribution curve shows that the pore diameter is of ca. 1.1 nm (Figure S2b), which confirms that microporous carbon can be prepared by the pyrolysis of PVDF through an activation-free method, as reported in the literature. The N_2 adsorption–desorption isotherm curve of Fe-F-C also shows a typical type IV characteristic, with a hierarchical tetramodal micro–meso–macro pore size distribution (Figure S2c,d). The specific surface area and pore volume of N-F-C and Fe-F-C are found to be 976.0 $m^2 \cdot g^{-1}$ and 0.1 $cm^3 \cdot g^{-1}$, and 951.2 $m^2 \cdot g^{-1}$ and 0.4 $cm^3 \cdot g^{-1}$, respectively.

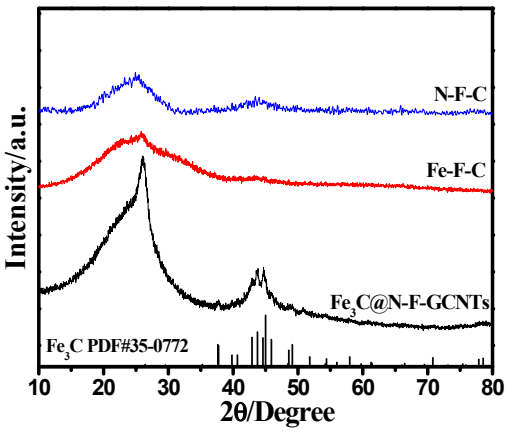

Figure 2. XRD patterns of Fe_3C@N-F-GCNTs, Fe-F-C, and N-F-C.

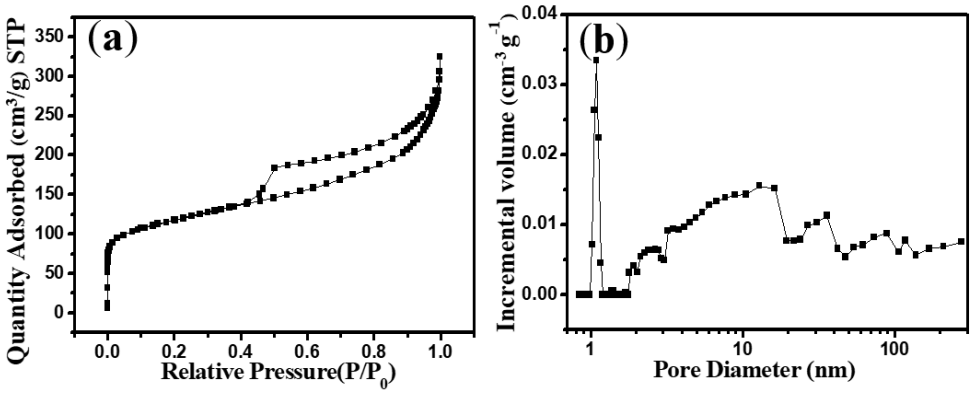

Figure 3. Nitrogen adsorption–desorption isotherms (**a**) and the corresponding pore-size distribution curve (**b**) of Fe_3C@N-F-GCNTs.

XPS analysis (Figure 4a) shows that Fe_3C@N-F-GCNTs is mainly composed of C (91.87 at.%), O (3.2 at.%), N (3.79 at.%), F (0.72 at. %), and Fe (0.42 at.%), confirming that N, O, F, and Fe were successfully incorporated into the carbon matrix (Table S1). The high-resolution N 1 s spectrum can be fitted to three peaks corresponding to oxidized-N (404.3 eV), graphite N (401.3 eV), pyrrole N (400.1 eV), and pyridine N/Fe-Nx (398.6 eV) (Figure 4b). Among them, graphite N (40.85%) and pyridine N (25.61%) are more catalytically active for ORR than pyrrole N (12.60%) and oxidized-N (20.94%) (Table S2). Figure 4c shows the high-resolution F 1 s spectrum; a main peak at 686.4 eV is attributable to the half-ion C-F bond. As described in the previous literature, charge redistribution induced by electronegativity can promote electrocatalytic reactions. Thus, a significant difference in electronegativity between the C and F atoms can promote electron transfer in the ORR

and OER. Figure 4d shows the XPS Fe 2p high-resolution spectrum of Fe_3C@N-F-GCNTs; no obvious Fe peaks are observed for the hybrid, suggesting that the formed carbon shell coatings are hindering core Fe_3C signals [35], in agreement with TEM results. The XPS analyses of Fe-F-C and N-F-C are also presented in Figures S3 and S4.

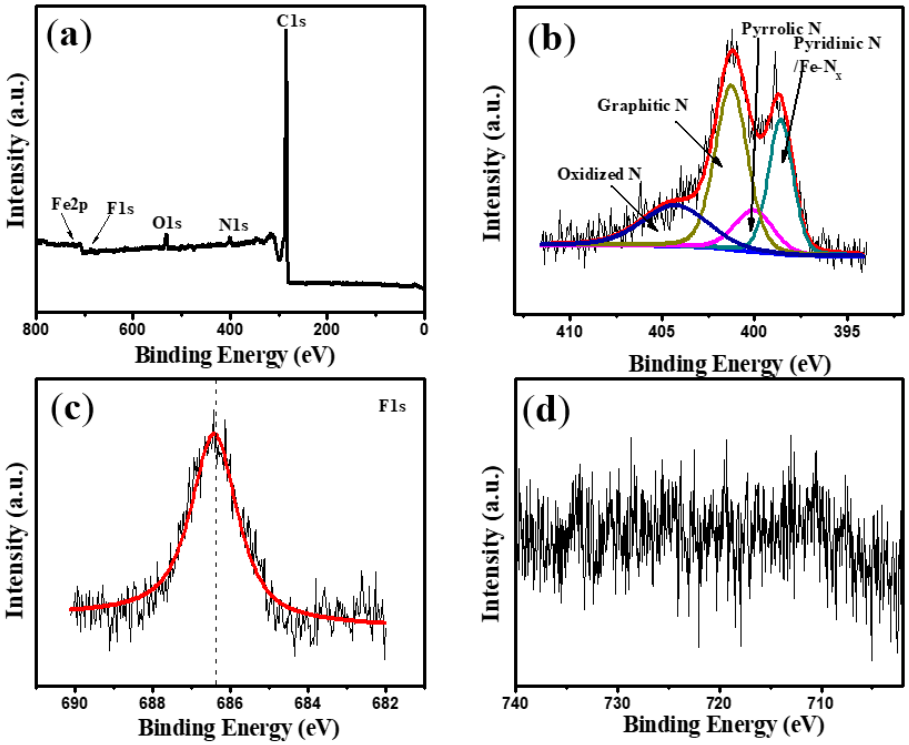

Figure 4. The XPS survey scan spectrum (**a**) and high-resolution deconvoluted spectra for N 1 s (**b**), F 1 s (**c**), and Fe 2p (**d**) of Fe_3C@N-F-GCNTs.

Figure 5a shows the LSV curves of Fe_3C@N-F-GCNTs, Fe-F-C, N-F-C, and 20 wt.% Pt/C in an O_2-gas-saturated 0.1 M KOH solution. The onset potential and half-wave potential of the catalysts for the ORR increase in the following order: Fe-F-C < N-F-C < Fe_3C@N-F-GCNTs. Among them, Fe_3C@N-F-GCNTs showed the best ORR catalytic performance, and its onset potential and half-wave potential were 0.972 V (vs. RHE) and 0.846 V (vs. RHE), respectively, which were 10 and 14 mV higher than those of commercial Pt/C, indicating better intrinsic catalytic activity than commercial Pt/C. Further, the diffusion limiting current density of Fe_3C@N-F-GCNTs at 0.6 V is 15% higher than that of 20 wt% Pt/C, indicating that its hierarchical framework containing graphene and carbon nanotubes is beneficial to the diffusion of reactants and products. The Tafel slope is an important parameter for assessing ORR activity. Figure 5b shows the Tafel slopes of Fe_3C@N-F-GCNTs, Fe-F-C, N-F-C, and 20 wt.% Pt/C, which are 54, 139, 86, and 68 $mV \cdot dec^{-1}$, respectively. The lower Tafel slope of Fe_3C@N-F-GCNTs indicates their high intrinsic catalytic activity.

To further understand the ORR process of Fe_3C@N-F-GCNTs, Fe-F-C, and N-F-C, we also performed RRDE measurements. As can be seen in Figure 5c,d, Fe_3C@N-F-GCNTs have the highest electron transfer number (~3.92) and the lowest peroxide yield (4–5%) (in the potential range of 0.3–0.6 V) when testing the ring current and the disk current; N-F-C has an electron transfer number of about 3.58 and a peroxide yield of 17–23%; Fe-F-C achieved the lowest electron transfer number (~3.4) and the highest peroxide yield (26–32% in the same voltage window).

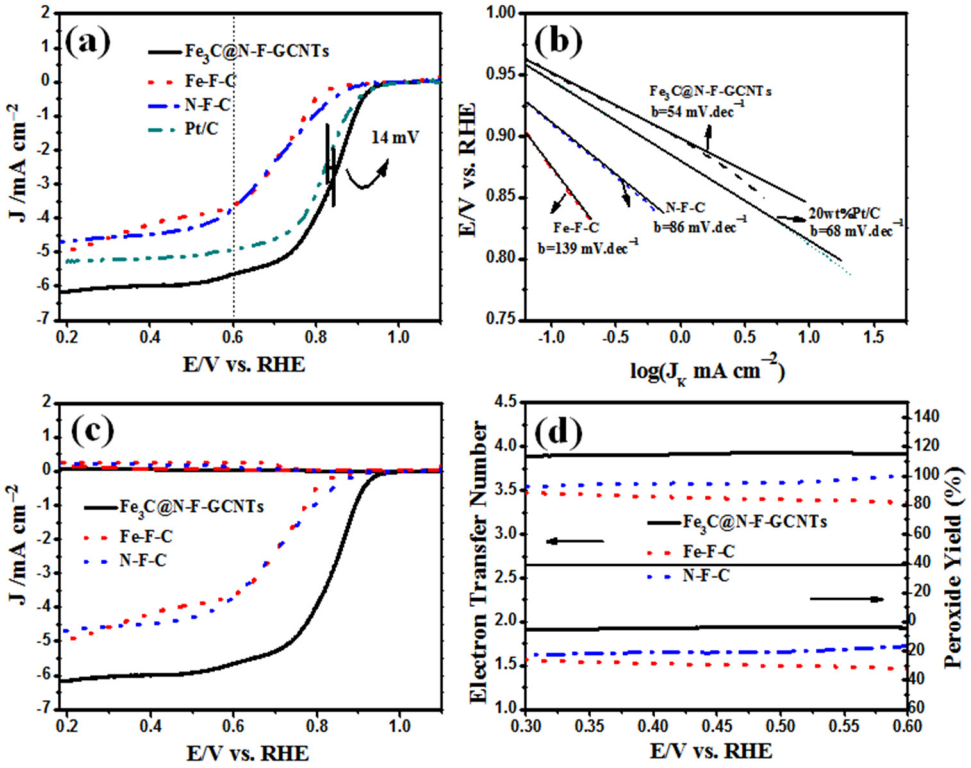

Figure 5. LSV curves of Fe_3C@N-F-GCNTs, Fe-F-C, N-F-C, and 20 wt.% Pt/C in O_2-saturated 0.1 M KOH solution at 1600 rpm (**a**); the corresponding Tafel slopes (**b**); RRDE voltammograms in 0.1 M KOH solution at a rotation rate of 1600 rpm (**c**); and the calculated peroxide yields (%) and electron transfer numbers (n) (**d**) of Fe_3C@N-F-GCNTs, Fe-F-C, and N-F-C.

Apart from high ORR activity, the excellent durability also plays a significant role for catalyst in practical applications. The durability of Fe_3C@N-F-GCNTs was assessed by current–time (i–t) chronoamperometry measurement in an O_2-saturated 0.10 M KOH aqueous solution with a rotating speed of 900 rpm at a constant cathodic voltage of 0.6 V. As a contrast, we also performed the same measurement for 20 wt.% Pt/C. As can be seen in Figure 6a, after continuous operation for 30,000 s, Fe_3C@N-F-GCNTs retain a relatively stable current density that only dropped by 16%; however, the Pt/C catalyst exhibits a faster and larger decay of ORR current density, illustrating the superior ORR durability of Fe_3C@N-F-GCNTs compared with commercial Pt/C.

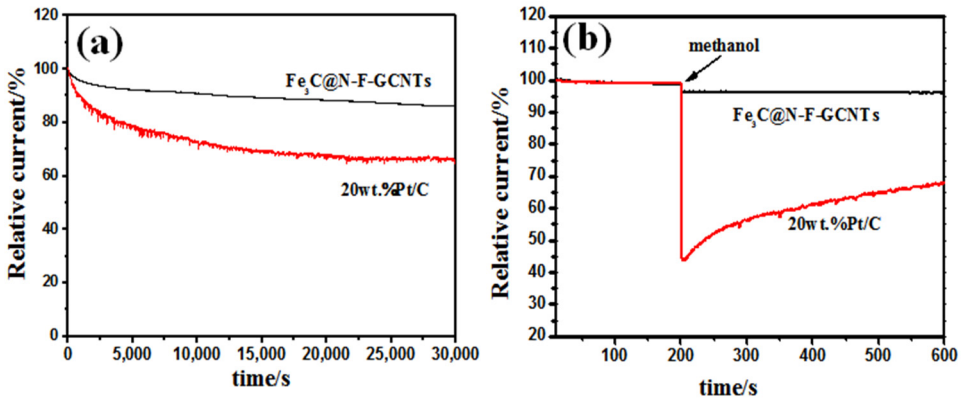

Figure 6. Chronoamperometric response for Fe_3C@N-F-GCNTs and Pt/C at 0.6 V (900 rpm) over a time span of 30,000 s (**a**); chronoamperometric responses for Fe_3C@N-F-GCNTs and Pt/C at 0.6 V with the addition of 3 M methanol at around 200 s (900 rpm) (**b**).

We also characterized the methanol positioning effect of the Fe_3C@N-F-GCNTs. As shown in Figure 6b, after introducing methanol at around 200 s, the Pt/C catalyst exhibits an obvious drop in current density, while Fe_3C@N-F-GCNTs achieve an excellent current retention ratio of 95%. This result suggests that the Fe_3C@N-F-GCNTs cathodic ORR catalyst can be used in methanol-based fuel cells as well.

To investigate the electrocatalytic OER activity of Fe_3C@N-F-GCNTs, the OER LSV test was performed at 1600 rpm in 0.1 M KOH electrolyte solution saturated with O_2. Similar tests were performed on Fe-F-C, N-F-C, and 20 wt.% IrO_2/C (Figure 7a) for comparison. Compared with the standard potential to split water (1.23 V), Fe_3C@N-F-GCNTs can afford 10 mA·cm^{-2} at a low overpotential (η) of 432 mV, which is close to the value for IrO_2/C (370 mV), while Fe-F-C and N-F-C reached 10 mA·cm^{-2} at higher overpotentials (η) of 656 and 621 mV, respectively.

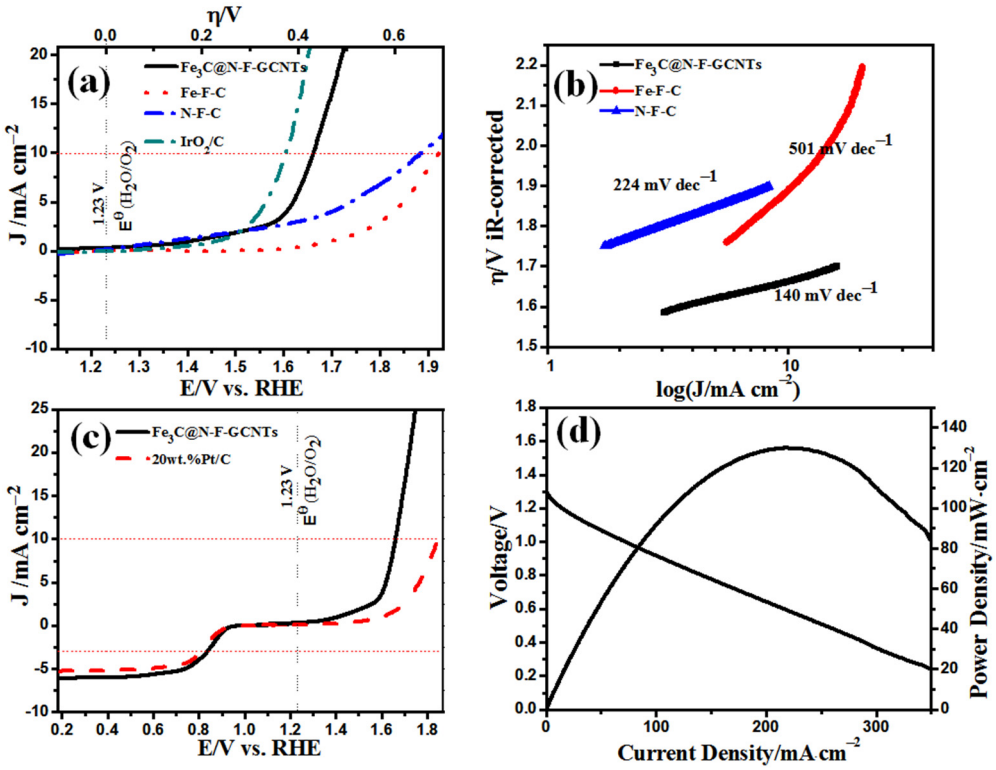

Figure 7. OER LSV curves of Fe_3C@N-F-GCNTs, Fe-F-C, N-F-C, and 20 wt.% IrO_2/C in O_2-saturated 0.1 M KOH electrolyte solution at 1600 rpm (**a**); the corresponding Tafel plots of Fe_3C@N-F-GCNTs, Fe-F-C, and N-F-C (**b**); the overall LSV curves of Fe_3C@N-F-GCNTs and 20 wt.% Pt/C for ORR and OER (**c**); discharge polarization and power plots of Zn–air batteries using Fe_3C@N-F-GCNTs as cathode (**d**).

To study the OER kinetics of the catalysts, we plotted their Tafel curves. As shown in Figure 7b, the Tafel slopes of Fe_3C@N-F-GCNTs, Fe-F-C, and N-F-C are ~140, ~501, and ~224 mV·dec^{-1}, respectively. Fe_3C@N-F-GCNTs showed the smallest Tafel slope, indicating that Fe_3C@N-F-GCNTs have excellent intrinsic OER catalytic activity.

For Fe_3C@N-F-GCNTs, an accelerated stability test was performed at room temperature to study the durability of the OER. As can be seen in Figure S5, after 200 repeated cycles, the η of Fe_3C@N-F-GCNTs increased by only 10 mV.

The bifunctional oxygen electrode electrocatalytic activity of the catalyst can be evaluated by measuring the potential difference (ΔE) between an OER potential at 10 mA·cm^{-2} and an ORR potential (−3 mA·cm^{-2}). The smaller the ΔE value, the higher the bifunctional electrocatalytic performance. The bifunctional electrocatalytic activity of the above catalyst is shown in Figure 7c. The ΔE value of Fe_3C@N-F-GCNTs is 0.827 V, and their ΔE value is comparable to or even smaller than that of most nonprecious metal-based ORR/OER

bifunctional electrocatalysts reported in literature (Table S3) [10,36–41], indicating their distinguished bifunctional activity. We also assembled a home-made Zn–air battery using Fe_3C@N-F-GCNTs as the cathode catalyst and Zn plate as the anode to further evaluate the possibility of practical application of Zn–air batteries. As can be seen in Figure 7d, the Zn–air battery with Fe_3C@N-F-GCNTs as cathode catalyst delivers a high power density up to 130 $mW \cdot cm^{-2}$, which ranks among the performance of the state-of-the-art carbon-based catalysts reported in the literatures (Table S4) [42–47]. Therefore, this catalyst is highly promising for practical applications in a Zn–air battery.

3. Materials and Methods

3.1. Materials

All purchased chemical reagents are of analytically pure grade and can be used directly. Melamine, PVDF, iron acetate, and concentrated sulfuric acid were purchased from Sinopharm Group (Shanghai, China). Nafion solution (5 wt.%) was purchased from Alfa Aesar. Commercial Pt/C (20 wt.%) was purchased from Johnson Matthey. IrO_2/C (20 wt.%) was prepared according to a previously reported method [48].

3.2. Preparation of the Catalysts

A total 2 g of melamine, 1 g of PVDF, and 0.4 g of iron acetate were added into 25 mL of deionized water; then, the suspension was magnetic stirred for 30 min and dried at 80 °C to obtain a catalyst precursor. The precursor was placed in a quartz boat and heat-treated at 900 °C for 2 h under argon atmosphere in a tube furnace. Followed by naturally cooling to room temperature, the sample was leached in a 1.0 M H_2SO_4 aqueous solution at 80 °C for 12 h and washed with deionized water and ethanol three times. Finally, the sample was dried at 60 °C for 12 h and subjected to secondary heat treatment under the same heat treatment conditions as described above; after cooling down to room temperature, the iron carbide nanoparticles embedded in edge-rich, N and F codoped graphene/carbon nanotubes hybrid (Fe_3C@N-F-GCNTs) was obtained. As a comparison, under the same conditions, we prepared Fe-F-C and N-F-C catalysts without melamine or iron acetate, respectively.

3.3. Physical Characterization

X-ray diffraction (XRD) patterns were recorded on a TD-3500 powder diffractometer (Tongda, Dandong, China). Transmission electron microscopy (TEM) images were acquired using a JEM-2100HR transmission electron microscope (JEOL, Tokyo, Japan). X-ray photoelectron spectroscopy (XPS) studies were conducted on an ESCALAB 250 X-ray photoelectron spectrometer (Thermo VG Scientific, Waltham, MA, USA). The specific surface area was analyzed using an adsorption–desorption isotherm curve obtained by a Micromeritics Tristar II 3020 (Micromeritics, Norcross, GA, USA).

3.4. Electrochemical Tests

Electrochemical tests were conducted in a conventional three-electrode electrolytic cell equipped with an electrochemical station (Ivium, Eindhoven, Netherlands). A Pt wire and an Hg/HgO electrode were used as the counter electrode and reference electrode, respectively. A catalyst-loaded glassy carbon electrode (GCE) (diameter, 5 mm) was used as the working electrode. The electrolyte was an aqueous 0.1 M KOH solution. All potentials in the text are quoted with respect to the reversible hydrogen electrode (RHE). The catalyst ink was prepared by dispersing 5 mg of active material in 1 mL Nafion ethanol solution (0.25 wt.%). Then, 20 μL homogeneous ink was dropped onto the GCE surface and dried in air at room temperature. Prior to testing, high-purity N_2 or O_2 gas was purged into the electrolyte solution to saturate it.

The number of electron transfers (n) per oxygen molecule for ORR of the catalyst is calculated by the Koutecky–Levich (K–L) equation [49]:

$$j^{-1} = j_k^{-1} + \left(0.62nFC_0D_0^{\frac{2}{3}}\gamma^{\frac{-1}{6}}\omega^{\frac{1}{2}}\right)^{-1} \quad (1)$$

where j is the current density, j_k is the kinetic current density, n is the number of electron transfers during the ORR reaction, F is the Faraday constant (F = 96485 C·mol^{-1}), C_0 is the volume concentration of O_2 ($C_0 = 1.2 \times 10^{-3}$ mol·L^{-1}), D_0 is the diffusion coefficient of O_2 ($D_0 = 1.9 \times 10^{-5}$ cm^2·s^{-1}), γ is the dynamic viscosity of the 0.1 M KOH solution (V = 0.01 cm^2·s^{-1}), and ω is the rotation speed of the disk.

The Tafel curve is obtained by mass-transfer-corrected linear sweep volt–ampere (LSV) data, where the kinetic current density is obtained by diffusion current correction of the current in the hybrid region, which is calculated as follows:

$$j_{kin} = \frac{jj_{diff}}{j_{diff} - j} \quad (2)$$

In the rotating ring disk (RRDE) test, the ring voltage was set to 1.5 V (vs. RHE), and the transferred electron number (n) and H_2O_2 yield could be calculated by the following formula [50]:

$$\begin{aligned} H_2O_2\% &= 200I_r(NI_d + I_r)^{-1} \\ n &= 4I_d\left(I_d + I_rN^{-1}\right)^{-1} \end{aligned} \quad (3)$$

where I_r is the ring current, I_d is the disk current, N is the capture rate of the Pt ring, and the value is 0.37.

4. Conclusions

In summary, we designed and successfully prepared a heterogeneous nano-oxygen double function of the Fe_3C@C nanoparticles embedded in edge-rich, N and F codoped graphene/carbon nanotubes frame structure catalyst (Fe_3C@N-F-GCNTs) by a simple, scalable method. The specific surface area of the catalyst is as high as 421 m^2·g^{-1} with a hierarchical micro–meso–macroporous structure. In alkaline electrolyte, Fe_3C@N-F-GCNTs exhibit outstanding ORR catalytic activity, and their half-wave voltage and diffusion limiting current density are 14 mV and 15% higher than those of the Pt/C catalyst, respectively, and the catalyst is also highly active for OER. Its overvoltage at 10 mA·cm^{-2} is only 432 mV, and its ΔE value is only 0.827 V, which is lower than that of commercial Pt/C and most other nonprecious metal bifunctional oxygen electrocatalysts. Furthermore, the home-made Zn–air battery with Fe_3C@N-F-GCNTs as the cathode catalyst delivers a high power density of up to 130 mW·cm^{-2}. Detailed studies show that the prominent catalytic performance of the material is due to: (1) a synergistic effect between various active sites (including Fe_3C@C, N and F dopant, Fe-N_x-C); (2) the surface etching on the carbon substrate could introduce more active edge sites; (3) high surface area and fast mass transfer caused by the hierarchical pore structure of the graphene/carbon nanotube framework. This work may provide a simple and scalable approach towards the preparation of 3D-etched graphene–nanotube hybrids for energy conversion and storage applications.

Supplementary Materials: The following supporting information can be downloaded at: https://www.mdpi.com/article/10.3390/catal12091023/s1, Figure S1. TEM images of Fe-F-C (a, b) and N-F-C (c, d); Figure S2. Nitrogen adsorption–desorption isotherms and pore-size distribution curve of N-F-C and Fe-F-C; Figure S3. XPS results for Fe-F-C: survey scan (a), high resolution deconvoluted spectra for F 1s (b), and Fe 2p (c); Figure S4. XPS results for N-F-C: survey scan (a), high resolution deconvoluted spectra for N 1s (b), and F 1s (c); Figure S5. OER LSV plots of Fe_3C@N-F-GCNTs before and after a potential cycling of 200 cycles (c); Table S1. Surface composition of Fe3C@N-F-GCNTs, Fe-F-C and N-F-C calculated from XPS results; Table S2. Distribution of each N species, obtained from the fitting results of N 1s XPS spectra (normalized to the surface N atoms of each material).

Table S3. Comparison of ORR and OER activity parameters with other recently reported highly active non-noble metal bifunctional electrocatalysts. Table S4. Comparison of the power density for Zn-air batteries.

Author Contributions: Methodology, X.Q. and Y.D.; date curation, X.Q., J.W., H.G. and W.X.; resources, X.C.; writing—original draft, X.Q.; writing—review and editing, X.Q. and S.L.; supervision, X.Q. and S.L. All authors have read and agreed to the published version of the manuscript.

Funding: This research was funded by the National natural science foundation of China (Project No. 21805034, 22005063), Natural Science Foundation of Guangdong Province (Project No. 2017A030310645), Innovation and Entrepreneurship Program for college students of Dongguan University of Technology (Project No. 202011819091, 202011819208) and Dongguan Science and Technology Commissioner Project (Project No. 20201800500252).

Data Availability Statement: Not applicable.

Conflicts of Interest: The authors declare no conflict of interest.

References

1. Yu, J.; Ran, R.; Zhong, Y.; Zhou, W.; Ni, M.; Shao, Z. Advances in Porous Perovskites: Synthesis and Electrocatalytic Performance in Fuel Cells and Metal–Air Batteries. *Energy Environ. Mater.* **2020**, *3*, 121–145. [CrossRef]
2. Wang, Y.; Chu, F.; Zeng, J.; Wang, Q.; Naren, T.; Li, Y.; Cheng, Y.; Lei, Y.; Wu, F. Single Atom Catalysts for Fuel Cells and Rechargeable Batteries: Principles, Advances, and Opportunities. *ACS Nano* **2021**, *15*, 210–239. [CrossRef] [PubMed]
3. Zhang, H.; Wang, X.; Yang, Z.; Yan, S.; Zhang, C.; Liu, S. Space-Confined Synthesis of Lasagna-like N-Doped Graphene-Wrapped Copper–Cobalt Sulfides as Efficient and Durable Electrocatalysts for Oxygen Reduction and Oxygen Evolution Reactions. *ACS Sustain. Chem. Eng.* **2020**, *8*, 1004–1014. [CrossRef]
4. Winter, M.; Brodd, R.J. What are batteries, fuel cells, and supercapacitors? *Chem. Rev.* **2004**, *104*, 4245–4270. [CrossRef] [PubMed]
5. Qu, K.; Zheng, Y.; Dai, S.; Qiao, S.Z. Graphene oxide-polydopamine derived N, S-codoped carbon nanosheets as superior bifunctional electrocatalysts for oxygen reduction and evolution. *Nano Energy* **2016**, *19*, 373–381. [CrossRef]
6. Chen, Z.; Higgins, D.; Yu, A.; Zhang, L.; Zhang, J. A review on non-precious metal electrocatalysts for PEM fuel cells. *Energy Environ. Sci.* **2011**, *4*, 3167. [CrossRef]
7. Qiao, X.; Peng, H.; You, C.; Liu, F.; Zheng, R.; Xu, D.; Li, X.; Liao, S. Nitrogen, phosphorus and iron doped carbon nanospheres with high surface area and hierarchical porous structure for oxygen reduction. *J. Power Source* **2015**, *288*, 253–260. [CrossRef]
8. Kim, J.; Zhou, R.; Murakoshi, K.; Yasuda, S. Advantage of semi-ionic bonding in fluorine-doped carbon materials for the oxygen evolution reaction in alkaline media. *Rsc. Adv.* **2018**, *8*, 14152–14156. [CrossRef] [PubMed]
9. Wang, L.; Wang, Y.; Wu, M.; Wei, Z.; Cui, C.; Mao, M.; Zhang, J.; Han, X.; Liu, Q.; Ma, J. Nitrogen, Fluorine, and Boron Ternary Doped Carbon Fibers as Cathode Electrocatalysts for Zinc-Air Batteries. *Small* **2018**, *14*, e1800737. [CrossRef]
10. Li, Z.; Gao, Q.; Liang, X.; Zhang, H.; Xiao, H.; Xu, P.; Liu, Z. Low content of Fe3C anchored on Fe,N,S-codoped graphene-like carbon as bifunctional electrocatalyst for oxygen reduction and oxygen evolution reactions. *Carbon* **2019**, *150*, 93–100. [CrossRef]
11. Murugesan, B.; Pandiyan, N.; Arumugam, M.; Veerasingam, M.; Sonamuthu, J.; Jeyaraman, A.R.; Samayanan, S.; Mahalingam, S. Two dimensional graphene oxides converted to three dimensional P, N, F and B, N, F tri-doped graphene by ionic liquid for efficient catalytic performance. *Carbon* **2019**, *151*, 53–67. [CrossRef]
12. Zhong, J.W.; Wu, T.; Wu, Q.; Du, S.; Chen, D.C.; Chen, B.; Chang, M.L.; Luo, X.H.; Liu, Y.L. N- and S- co-doped graphene sheet-encapsulated Co_9S_8 nanomaterials as excellent electrocatalysts for the oxygen evolution reaction. *J. Power Source* **2019**, *417*, 90–98. [CrossRef]
13. Zheng, X.J.; Wu, J.; Cao, X.C.; Abbott, J.; Jin, C.; Wang, H.B.; Strasser, P.; Yang, R.Z.; Chen, X.; Wu, G. N-, P-, and S-doped graphene-like carbon catalysts derived from onium salts with enhanced oxygen chemisorption for Zn-air battery cathodes. *Appl. Catal. B-Environ.* **2019**, *241*, 442–451. [CrossRef]
14. Wu, H.; Wang, J.; Wang, G.; Cai, F.; Ye, Y.; Jiang, Q.; Sun, S.; Miao, S.; Bao, X. High-performance bifunctional oxygen electrocatalyst derived from iron and nickel substituted perfluorosulfonic acid/polytetrafluoroethylene copolymer. *Nano Energy* **2016**, *30*, 801–809. [CrossRef]
15. Qiao, X.; Liao, S.; Wang, G.; Zheng, R.; Song, H.; Li, X. Simultaneous doping of nitrogen and fluorine into reduced graphene oxide: A highly active metal-free electrocatalyst for oxygen reduction. *Carbon* **2016**, *99*, 272–279. [CrossRef]
16. Zhang, H.J.; Yao, S.W.; Geng, J.; Ma, Z.F.; Yang, J.H. Oxygen reduction reaction with efficient, metal-free nitrogen, fluoride-codoped carbon electrocatalysts derived from melamine hydrogen fluoride salt. *J. Colloid Interface Sci.* **2019**, *535*, 436–443. [CrossRef]
17. Gong, T.L.; Qi, R.Y.; Liu, X.D.; Li, H.; Zhang, Y.M. N, F-Codoped Microporous Carbon Nanofibers as Efficient Metal-Free Electrocatalysts for ORR. *Nano-Micro. Lett.* **2019**, *11*, 9. [CrossRef]
18. Xia, W.; Mahmood, A.; Liang, Z.; Zou, R.; Guo, S. Earth-Abundant Nanomaterials for Oxygen Reduction. *Angew. Chem. Int. Ed.* **2016**, *55*, 2650–2676. [CrossRef]
19. Li, Y.-F.; Liu, Z.-P. Structure and water oxidation activity of 3d metal oxides. *WIREs Comput. Mol. Sci.* **2016**, *6*, 47–64. [CrossRef]

20. Zhang, B.; Zheng, X.; Voznyy, O.; Comin, R.; Bajdich, M.; García-Melchor, M.; Han, L.; Xu, J.; Liu, M.; Zheng, L.; et al. Homogeneously dispersed multimetal oxygen-evolving catalysts. *Science* **2016**, *352*, 333–337. [CrossRef]
21. Kairi, M.I.; Khavarian, M.; Bakar, S.A.; Vigolo, B.; Mohamed, A.R. Recent trends in graphene materials synthesized by CVD with various carbon precursors. *J. Mater. Sci.* **2017**, *53*, 851–879. [CrossRef]
22. Kumar, M.; Ando, Y. Chemical Vapor Deposition of Carbon Nanotubes: A Review on Growth Mechanism and Mass Production. *J. Nanosci. Nanotechnol.* **2010**, *10*, 3739–3758. [CrossRef] [PubMed]
23. Askari, M.B.; Salarizadeh, P.; Di Bartolomeo, A.; Sen, F. Enhanced electrochemical performance of $MnNi_2O_4$/rGO nanocomposite as pseudocapacitor electrode material and methanol electro-oxidation catalyst. *Nanotechnology* **2021**, *32*, 325707. [CrossRef] [PubMed]
24. Fu, K.; Wang, Y.; Mao, L.; Yang, X.; Jin, J.; Yang, S.; Li, G. Strongly coupled Co, N co-doped carbon nanotubes/graphene-like carbon nanosheets as efficient oxygen reduction electrocatalysts for primary Zinc-air battery. *Chem. Eng. J.* **2018**, *351*, 94–102. [CrossRef]
25. Dou, S.; Tao, L.; Huo, J.; Wang, S.; Dai, L. Etched and doped Co_9S_8/graphene hybrid for oxygen electrocatalysis. *Energy Environ. Sci.* **2016**, *9*, 1320–1326. [CrossRef]
26. Tang, C.; Wang, H.F.; Chen, X.; Li, B.Q.; Hou, T.Z.; Zhang, B.; Zhang, Q.; Titirici, M.M.; Wei, F. Topological Defects in Metal-Free Nanocarbon for Oxygen Electrocatalysis. *Adv. Mater.* **2016**, *28*, 6845–6851. [CrossRef]
27. Tao, L.; Wang, Q.; Dou, S.; Ma, Z.L.; Huo, J.; Wang, S.Y.; Dai, L.M. Edge-rich and dopant-free graphene as a highly efficient metal-free electrocatalyst for the oxygen reduction reaction. *Chem. Commun.* **2016**, *52*, 2764–2767. [CrossRef]
28. Tang, C.; Zhang, Q. Nanocarbon for Oxygen Reduction Electrocatalysis: Dopants, Edges, and Defects. *Adv. Mater.* **2017**, *29*, 1604103. [CrossRef]
29. Xu, B.; Hou, S.; Chu, M.; Cao, G.; Yang, Y. An activation-free method for preparing microporous carbon by the pyrolysis of poly(vinylidene fluoride). *Carbon* **2010**, *48*, 2812–2814. [CrossRef]
30. Yang, W.; Liu, X.; Yue, X.; Jia, J.; Guo, S. Bamboo-like carbon nanotube/Fe_3C nanoparticle hybrids and their highly efficient catalysis for oxygen reduction. *J. Am. Chem. Soc.* **2015**, *137*, 1436–1439. [CrossRef]
31. Yang, W.; Yue, X.; Liu, X.; Chen, L.; Jia, J.; Guo, S. Superior oxygen reduction electrocatalysis enabled by integrating hierarchical pores, Fe3C nanoparticles and bamboo-like carbon nanotubes. *Nanoscale* **2016**, *8*, 959–964. [CrossRef] [PubMed]
32. Zhong, G.; Wang, H.; Yu, H.; Peng, F. Nitrogen doped carbon nanotubes with encapsulated ferric carbide as excellent electrocatalyst for oxygen reduction reaction in acid and alkaline media. *J. Power Source* **2015**, *286*, 495–503. [CrossRef]
33. Palaniselvam, T.; Aiyappa, H.B.; Kurungot, S. An efficient oxygen reduction electrocatalyst from graphene by simultaneously generating pores and nitrogen doped active sites. *J. Mater. Chem.* **2012**, *22*, 23799–23805. [CrossRef]
34. Chen, L.; Chen, Z.; Kuang, Y.; Xu, C.; Yang, L.; Zhou, M.; He, B.; Jing, M.; Li, Z.; Li, F.; et al. Edge-Rich Quasi-Mesoporous Nitrogen-Doped Carbon Framework Derived from Palm Tree Bark Hair for Electrochemical Applications. *ACS Appl. Mater. Interfaces* **2018**, *10*, 27047–27055. [CrossRef] [PubMed]
35. Hou, Y.; Huang, T.; Wen, Z.; Mao, S.; Cui, S.; Chen, J. Metal−Organic Framework-Derived Nitrogen-Doped Core-Shell-Structured Porous Fe/Fe_3C@C Nanoboxes Supported on Graphene Sheets for Efficient Oxygen Reduction Reactions. *Adv. Energy Mater.* **2014**, *4*, 1400337. [CrossRef]
36. Zhao, J.Y.; Wang, R.; Wang, S.; Lv, Y.R.; Xu, H.; Zang, S.Q. Metal-organic framework-derived Co_9S_8 embedded in N, O and S-tridoped carbon nanomaterials as an efficient oxygen bifunctional electrocatalyst. *J. Mater. Chem. A* **2019**, *7*, 7389–7395. [CrossRef]
37. Ranjbar Sahraie, N.; Paraknowitsch, J.P.; Göbel, C.; Thomas, A.; Strasser, P. Noble-Metal-Free Electrocatalysts with Enhanced ORR Performance by Task-Specific Functionalization of Carbon using Ionic Liquid Precursor Systems. *J. Am. Chem. Soc.* **2014**, *136*, 14486–14497. [CrossRef]
38. Tian, G.L.; Zhang, Q.; Zhang, B.S.; Jin, Y.G.; Huang, J.Q.; Su, D.S.; Wei, F. Toward Full Exposure of "Active Sites": Nanocarbon Electrocatalyst with Surface Enriched Nitrogen for Superior Oxygen Reduction and Evolution Reactivity. *Adv. Funct. Mater.* **2014**, *24*, 5956–5961. [CrossRef]
39. Ban, J.J.; Xu, G.C.; Zhang, L.; Xu, G.; Yang, L.J.; Sun, Z.P.; Jia, D.Z. Efficient Co-N/PC@CNT bifunctional electrocatalytic materials for oxygen reduction and oxygen evolution reactions based on metal-organic frameworks. *Nanoscale* **2018**, *10*, 9077–9086. [CrossRef]
40. Qiao, X.; Jin, J.; Luo, J.; Fan, H.; Cui, L.; Wang, W.; Liu, D.; Liao, S. In-situ formation of N doped hollow graphene Nanospheres/CNTs architecture with encapsulated Fe_3C@C nanoparticles as efficient bifunctional oxygen electrocatalysts. *J. Alloys Compd.* **2020**, *828*, 154238. [CrossRef]
41. Xiao, J.; Chen, C.; Xi, J.; Xu, Y.; Xiao, F.; Wang, S.; Yang, S. Core–shell Co@ Co_3O_4 nanoparticle-embedded bamboo-like nitrogen-doped carbon nanotubes (BNCNTs) as a highly active electrocatalyst for the oxygen reduction reaction. *Nanoscale* **2015**, *7*, 7056–7064. [PubMed]
42. Li, Y.H.; Zang, K.T.; Duan, X.Z.; Luo, J.; Chen, D. Boost oxygen reduction reaction performance by tuning the active sites in Fe-N-P-C catalysts. *J. Energy Chem.* **2021**, *55*, 572–579. [CrossRef]
43. Li, T.F.; Li, M.; Zhang, M.R.; Li, X.; Liu, K.H.; Zhang, M.Y.; Liu, X.; Sun, D.M.; Xu, L.; Zhang, Y.W.; et al. Immobilization of Fe3N nanoparticles within N-doped carbon nanosheet frameworks as a high-efficiency electrocatalyst for oxygen reduction reaction in Zn-air batteries. *Carbon* **2019**, *153*, 364–371. [CrossRef]

44. Chen, D.; Li, G.F.; Chen, X.; Li, C.J.; Zhang, Y.C.; Hu, J.; Yu, J.H.; Yu, L.Y.; Dong, L.F. CoFeNi/N-codoped carbon nanotubes with small diameters derived from spherical Prussian blue analog as bifunctional oxygen electrocatalysts for rechargeable Zn-air batteries. *J. Alloys Compd.* **2022**, *910*, 164964. [CrossRef]
45. Deng, Y.J.; Tian, X.L.; Chi, B.; Wang, Q.Y.; Ni, W.P.; Gao, Y.; Liu, Z.E.; Luo, J.M.; Lin, C.X.; Ling, L.M.; et al. Hierarchically open-porous carbon networks enriched with exclusive Fe-N-x active sites as efficient oxygen reduction catalysts towards acidic H-2-O-2 PEM fuel cell and alkaline Zn-air battery. *Chem. Eng. J.* **2020**, *390*, 124479. [CrossRef]
46. Wang, Q.; Ji, Y.; Lei, Y.; Wang, Y.; Wang, Y.; Li, Y.; Wang, S. Pyridinic-N-Dominated Doped Defective Graphene as a Superior Oxygen Electrocatalyst for Ultrahigh-Energy-Density Zn–Air Batteries. *ACS Energy Lett.* **2018**, *3*, 1183–1191. [CrossRef]
47. Yang, T.F.; Chen, Y.; Liu, Y.; Liu, X.P.; Gao, S.Y. Self-sacrificial template synthesis of Fe, N co-doped porous carbon as efficient oxygen reduction electrocatalysts towards Zn-air battery application. *Chin. Chem. Lett.* **2022**, *33*, 2171–2177. [CrossRef]
48. Prabu, M.; Ramakrishnan, P.; Shanmugam, S. CoMn2O4 nanoparticles anchored on nitrogen-doped graphene nanosheets as bifunctional electrocatalyst for rechargeable zinc–air battery. *Electrochem. Commun.* **2014**, *41*, 59–63. [CrossRef]
49. Liang, Y.; Li, Y.; Wang, H.; Zhou, J.; Wang, J.; Regier, T.; Dai, H. Co_3O_4 nanocrystals on graphene as a synergistic catalyst for oxygen reduction reaction. *Nat. Mater.* **2011**, *10*, 780–786. [CrossRef]
50. Liang, Y.; Wang, H.; Zhou, J.; Li, Y.; Wang, J.; Regier, T.; Dai, H. Covalent hybrid of spinel manganese–cobalt oxide and graphene as advanced oxygen reduction electrocatalysts. *J. Am. Chem. Soc.* **2012**, *134*, 3517–3523. [CrossRef]